

Physics and Applications of Metallic Magnetic Calorimeters

S. Kempf¹  · A. Fleischmann¹ · L. Gastaldo¹ · C. Enss¹

Received: 4 November 2017 / Accepted: 3 March 2018 / Published online: 12 March 2018
© Springer Science+Business Media, LLC, part of Springer Nature 2018

Abstract Metallic magnetic calorimeters (MMCs) are calorimetric low-temperature particle detectors that are currently strongly advancing the state of the art in energy-dispersive single particle detection. They are typically operated at temperatures below 100 mK and make use of a metallic, paramagnetic temperature sensor to transduce the temperature rise of the detector upon the absorption of an energetic particle into a change of magnetic flux which is sensed by a superconducting quantum interference device. This outstanding interplay between a high-sensitivity thermometer and a near quantum-limited amplifier results in a very fast signal rise time, an excellent energy resolution, a large dynamic range, a quantum efficiency close to 100% as well as an almost ideal linear detector response. For this reason, a growing number of groups located all over the world is developing MMC arrays of various sizes which are routinely used in a variety of applications. Within this paper, we briefly review the state of the art of metallic magnetic calorimeters. This includes a discussion of the detection principle, sensor materials and detector geometries, readout concepts, the structure of modern detectors as well as the state-of-the-art detector performance.

Keywords Metallic magnetic calorimeters · Low-temperature detectors · Microcalorimeters

✉ S. Kempf
sebastian.kempf@kip.uni-heidelberg.de

¹ Kirchhoff-Institute for Physics, Heidelberg University, Im Neuenheimer Feld 227, 69120 Heidelberg, Germany

1 Introduction

Metallic magnetic calorimeters (MMCs) [1] form together with superconducting transition edge sensors (TESs) [2] and semiconductor thermistors [3] a class of ultra-sensitive energy-dispersive low-temperature particle detectors which are presently strongly advancing the state of the art in single particle detection. They are used in a variety of applications including atomic and nuclear physics, searches for dark matter and the neutrinoless double beta decay, direct neutrino mass determination, nuclear safeguards, Q-spectroscopy, radionuclide metrology, X-ray astronomy, laboratory astrophysics, heavy ion physics, mass spectrometry and material analysis. For a description of the recent progress in these versatile fields, we refer to the proceedings of the international workshop on low-temperature detectors.

MMCs are typically operated at temperatures $T < 100$ mK and usually consist of a massive particle absorber that is suited for the particles to be detected and that is in tight thermal contact to a paramagnetic temperature sensor. The latter is placed in a weak magnetic field to create a temperature dependent sensor magnetization. The sensor is weakly coupled to a thermal bath kept at constant temperature to allow the detector to take a well-defined state in the absence of an energy input. According to the calorimetric detection principle, a temperature rise of the detector upon the deposition of energy in the absorber leads to a change of sensor magnetization. The latter can be precisely measured as a change of magnetic flux using a superconducting quantum interference device (SQUID).

2 Detector Basics

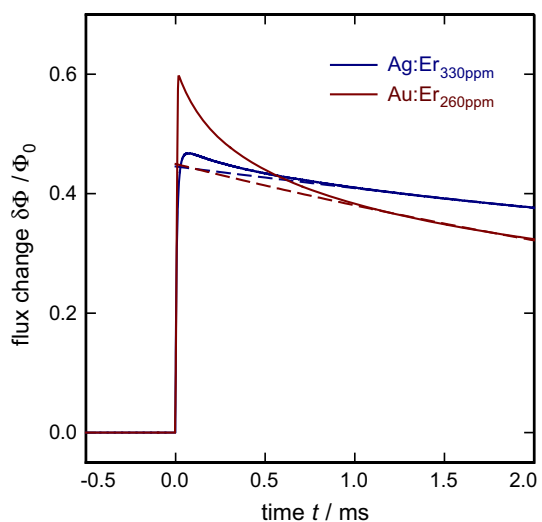
2.1 Sensor Materials

The sensor materials which are presently mostly used for MMCs are dilute paramagnetic alloys consisting of a Au or Ag host that is doped with a few hundred ppm erbium. At sufficiently low Er concentrations, both alloys form a solid solution where Er^{3+} ions substitute ions of the host material at regular lattice sites [4]. The magnetic moment of the Er ions results from the electrons of the $4f$ -shell which is located deep inside the Er ion. For this reason, the interaction of the $4f$ -electrons with the conduction electrons of the host material and with the crystal field is greatly reduced. Consequently, the magnetic moment of the Er ions can be calculated from the orbital angular momentum \mathbf{L} , the spin \mathbf{S} and the total angular momentum \mathbf{J} that can be derived according to Hund's rules. At high temperatures, $T > 100$ K, the magnetization of both alloys can be described by the magnetic moment $\boldsymbol{\mu} = g_J \mu_B \mathbf{J}$ [5]. Here, $g_J = 6/5$ denotes the Landé factor, $J = 15/2$ and μ_B is Bohr's magneton. At lower temperatures, $T < 100$ K, the crystal field needs to be included [6]. It induces a splitting of the 16-fold degeneracy of the ground state of the Er ion into a series of multiplets. The lowest Γ_7 -Kramers doublet is well separated by an energy gap ΔE from the higher multiplets. This energy gap is $\Delta E/k_B = 17$ K for Au:Er and $\Delta E/k_B = 25$ K for Ag:Er [7]. Consequently, at the typical operation temperatures of MMCs and in small

magnetic fields, both alloys effectively behave as a two-level system with an effective spin $\tilde{S} = 1/2$ and an isotropic g -factor $g = 6.8$ [5,8].

The thermodynamic properties of the sensor material, i.e., the temperature and magnetic field dependence of the magnetization and the specific heat, can be calculated with confidence using mean-field or Monte-Carlo simulations [1,9]. For performing these calculations, both the magnetic dipole–dipole interaction and the Ruderman–Kittel–Kasuja–Yoshida (RKKY) interaction need to be included. While the strength of the dipole–dipole interaction is equal for both alloys, the strength of the RKKY interaction is different. This results from the difference in the exchange energy J_{RKKY} . It is $J_{\text{RKKY}} = (0.10 \pm 0.02)$ eV for Au:Er and $J_{\text{RKKY}} = (0.16 \pm 0.03)$ eV for Ag:Er [8]. The strength of the RKKY interaction is therefore about a factor of 3 larger for Ag:Er as compared to Au:Er resulting in an overall signal size that is slightly reduced. However, this drawback is compensated by the fact that Ag has in contrast to Au no nuclear quadrupole moment. Since the Er ions distort the lattice symmetry of the host material and create strong electric field gradients at the sites of the surrounding nuclei of the host material due to the different charge distribution of the Er ions, the energy eigenstates of Au:Er are no longer degenerate and a nuclear quadrupole splitting is induced. Consequently, Au:Er carries an additional heat capacity [9] due to the nuclear quadrupole splitting. This splitting results in an initial fast signal decay (see Fig. 1). In contrast, Ag has a nuclear moment $I = 1/2$ and therefore doesn't carry a nuclear quadrupole moment. Consequently, there is no initial fast signal decay (see Fig. 1) and the specific heat is reduced. Overall, the absence of a fast signal decay leads to a comparable performance as for Au:Er. However, the signal shape is simpler and results in an overall improved energy resolution due to the longer signal decay time τ_{decay} [see Eq. (3)].

Fig. 1 Comparison between the detector response upon the absorption of 5.9keV photons using detectors that are equipped with a Au:Er or Ag:Er sensor. The solid lines indicate a single-exponential signal decay that was fitted to the measured signals for $t > 1$ ms (Color figure online)



2.2 Detector Geometries

During the last decade, a variety of detector geometries and coupling schemes between detector and SQUID have been developed. They are summarized, for example, in [1]. Figure 2 shows two transformer-coupled detector geometries that represent the state of the art. Two pickup coils, each having the inductance L_p , are connected in parallel with the input coil with inductance L_{in} of the current-sensing SQUID to form a superconducting flux transformer. This arrangement allows not only to spatially separate detector and SQUID to reduce the power dissipation in the vicinity of the detector but also to store a persistent current inside the pickup coils to create the bias magnetic field for magnetizing the temperature sensors. The latter can be injected by using a persistent current switch which is embedded within the circuit (see Sect. 4). The interconnections of both pickup coils are chosen such that both pixels show signals with different polarity. For this reason, the polarity of the SQUID signal allows to distinguish the pixel in which an event occurred. Another positive consequence of this wiring is that the detector forms a first-order gradiometer such that homogeneous variations of external magnetic background fields as well as fluctuations of the temperature of the heat bath are effectively canceled out.

The detector geometries shown in Fig. 2 differ from each other by the shape of the pickup coil as well as the placement of the sensor material. Figure 2 (left) shows a geometry using meander-shaped pickup coils [10, 11] that are each covered with a planar temperature sensor. Here, the persistent current creating the bias magnetic field flows within a single superconducting layer; thus, vertical interconnects with

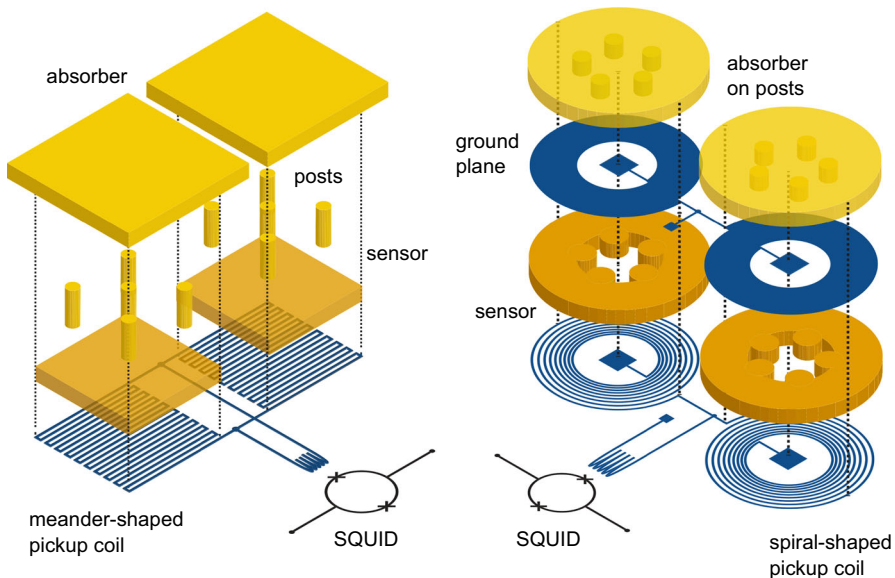


Fig. 2 Schematics of two state-of-the-art transformer-coupled detector geometries using (Left) meander-shaped and (Right) spiral-shaped pickup coils (Color figure online)

high critical current aren't of major importance. This geometry can hence be easily fabricated. But since the sensor material is placed only on top of the pickup coils, the magnetic filling factor F can at most approach $F \simeq 0.5$. In addition, the magnetic field within the sensor volume is inhomogeneous. In contrast, Fig. 2 (right) shows an alternative detector geometry for which the sensor material is sandwiched between a superconducting spiral-shaped coil and a superconducting ground plane [12, 13]. This results in a filling factor that can potentially reach the maximum value $F \simeq 1$ as well as a more homogeneous magnetic field within the sensor volume.

2.3 Noise Contributions and Energy Resolution

The energy resolution ΔE_{FWHM} of a metallic magnetic calorimeter can be calculated within the framework of optimal filtering via the relation [1]

$$\Delta E_{\text{FWHM}} = 2\sqrt{2 \ln 2} \left(\int_0^\infty \frac{|\tilde{p}(f)|^2}{S_{E_z, \text{tot}}} df \right)^{-1/2}. \quad (1)$$

Here, $\tilde{p}(f) \simeq \tau_{\text{decay}} / \sqrt{1 + 2\pi f \tau_{\text{rise}}} \sqrt{1 + 2\pi f \tau_{\text{decay}}}$ is an adequately normalized detector responsivity where τ_{rise} and τ_{decay} denote the signal rise and decay time of the detector. Furthermore, $\sqrt{S_{E_z, \text{tot}}}$ is the apparent noise of the energy content of the temperature sensor, i.e., the spin system, that is composed of four major noise contributions. These are (i) thermodynamic energy fluctuations between the absorber with heat capacity C_{abs} , the sensor with heat capacity C_{sens} and the heat bath, (ii) magnetic Johnson noise due to the thermal motions of electrons within metallic detector components, (iii) readout noise and (iv) sensor intrinsic $1/f$ -like excess noise. The thermodynamical energy fluctuations (TEF) can be calculated using the relation

$$S_{E_z, \text{TEF}} = 4k_B C_{\text{sens}} T^2 \left[(1 - \beta) \frac{\tau_{\text{rise}}}{1 + (2\pi f \tau_{\text{rise}})^2} + \beta \frac{\tau_{\text{decay}}}{1 + (2\pi f \tau_{\text{decay}})^2} \right] \quad (2)$$

with $\beta = C_{\text{sens}} / (C_{\text{sens}} + C_{\text{abs}})$. They represent an intrinsic noise contribution of the detector that leads to a fundamental limit of the energy resolution. For an optimized detector with $C_{\text{abs}} = C_{\text{sens}}$, this limit is given by

$$\Delta E_{\text{FWHM}} = 2.35 \sqrt{4k_B T^2 C_{\text{sens}}} \left(4 \frac{\tau_{\text{rise}}}{\tau_{\text{decay}}} \right)^{1/4}. \quad (3)$$

Here, T denotes the operation temperature and k_B is Boltzmann's constant. The magnetic Johnson noise obeys the equation $\sqrt{S_{\Phi, J}} = \mathcal{C} \sqrt{\sigma k_B T}$ where σ denotes the electrical conductivity of the metallic detector component and the geometry dependent factor \mathcal{C} quantifies the coupling to the pickup coil. The latter can easily be calculated for a given detector configuration by means of finite-element simulations. The contribution of readout noise is commonly expressed as the coupled energy resolution ε_c that is related to the magnetic flux noise $\sqrt{S_{\Phi, \text{SQ}}}$ of the SQUID via the relation

$\varepsilon_c = S_{\phi, \text{SQ}} / 2k_{\text{in}}^2 L_s$. Here, k_{in} is the magnetic coupling factor between the SQUID and its input coil. The origin of the sensor intrinsic $1/f$ -like noise contribution is still not fully understood. It is empirically found to be independent of temperature between 20 mK and 4.2 K and to be proportional to the number of Er ions inside the sensor. It can be described by attributing a fluctuating magnetic moment with a noise density of $S_m \simeq 0.1 \mu_B / f^{0.8 \dots 1}$ to every ion where the noise exponent seems to somehow depend on the detector geometry [13].

3 Detector Readout

Equation (1) shows that the energy resolution ΔE_{FWHM} of a metallic magnetic calorimeter is determined by the detector responsivity as well as the overall noise spectrum. While the thermodynamic energy fluctuations, the magnetic Johnson noise and the sensor intrinsic $1/f$ -noise contribution are set by the detector geometry as well as the choice of the sensor and absorber materials, the readout noise is in first-order independent of the detector configuration. Nevertheless, it strongly affects the overall noise spectrum and often sets a limit to the energy resolution. Figure 3 (left) shows as an example the calculated noise budget of an optimized soft X-ray detector assuming a SQUID with a white noise contribution $\varepsilon_{c,w} = 2h$ as well as a $1/f$ -noise contribution with a corner frequency $f_c = 100$ Hz. Obviously, the SQUID white noise contribution dominates the overall noise spectrum for frequencies above several kilohertz and is about an order of magnitude higher than the high-frequency plateau of the thermodynamic energy fluctuations or the sensor intrinsic excess noise. Consequently, SQUID white noise limits the overall signal-to-noise ratio and hence the energy resolution of the detector. Moreover, depending on its actual amplitude as well as the amplitude of

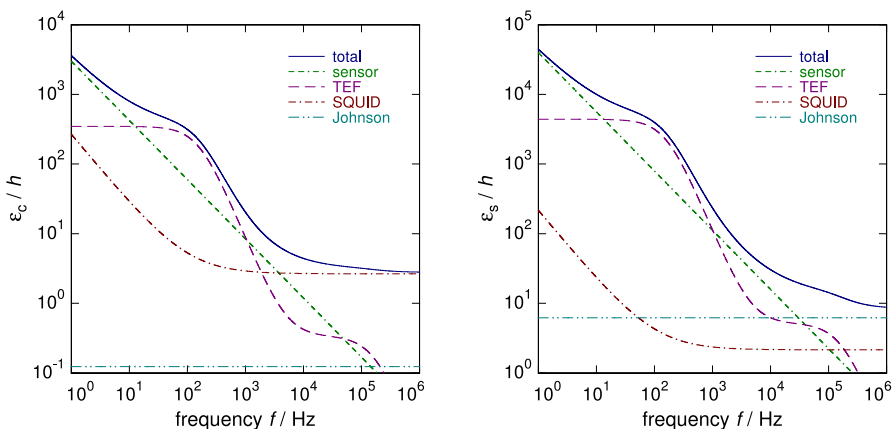


Fig. 3 Calculated noise budget of a detector that is optimized for high-resolution soft X-ray spectroscopy. The detector is assumed to comprise a single meander-shaped pickup coil that is covered by a planar temperature sensor made of Au:Er and to be read out by a SQUID via (Left) transformer-coupling and (Right) direct coupling. The SQUID is assumed to have a coupled or intrinsic energy resolution, respectively, of $\varepsilon_{c,w} = 2h$ in the white noise region and a corner frequency $f_c = 100$ Hz of true $1/f$ noise (Color figure online)

the sensor intrinsic noise, low-frequency SQUID noise might also affect the energy resolution.

When analyzing the influence of readout noise on the energy resolution ΔE_{FWHM} , we have to distinguish two situations. First, we can assume a given SQUID and search for a detector geometry minimizing the energy resolution. This strategy is mainly used when designing a new detector and allows to achieve the best energy resolution for a given SQUID. Second, we can consider an existing detector and investigate the dependence of the energy resolution on the SQUID parameters. In [14] we used the first approach to analyze the influence of the coupled energy sensitivity $\varepsilon_c(f)$ on the energy resolution of a MMC and to derive an upper limit for the white and low-frequency noise contribution of the SQUID that still allows to build a soft X-ray detector with sub-eV energy resolution. We assumed a state-of-the-art soft X-ray detector consisting of a single meander-shaped pickup coil with $6\text{ }\mu\text{m}$ pitch and $3\text{ }\mu\text{m}$ linewidth, a planar Au:Er temperature sensor lying on top of the pickup coil as well as a particle absorber having a heat capacity of $C_{\text{abs}} = 0.15\text{ pJ/K}$ at an operation temperature of $T = 30\text{ mK}$ as well as a signal rise time $\tau_{\text{rise}} = 1\text{ }\mu\text{s}$, a signal decay time $\tau_{\text{decay}} = 1\text{ ms}$ and a parasitic inductance $L_w = 500\text{ pH}$ within the superconducting flux transformer. In contrast to previous works [1, 13], we assumed that the input coil inductance of the SQUID can be varied within a certain range while maintaining a constant magnetic flux coupling factor to the SQUID. It turned out that a SQUID with a white noise contribution $\varepsilon_{c,w} < 30\text{ }h$ and a $1/f$ corner frequency $f_c < 100\text{ Hz}$ is required to build a detector with sub-eV energy resolution. Although this demand can be slightly relaxed when using a detector geometry with higher filling factor, e.g., a spiral-shaped pickup coil with superconducting ground plane, this statement is generally valid and makes clear that a SQUID with near quantum-limited noise performance is required to build a detector with sub-eV energy resolution. The calculations additionally showed that impedance matching between the detector and the input coil of the SQUID is a crucial requirement. The optimal value of the input coil inductance of a detector with sub-eV energy resolution ranges between 800 and 900 pH.

When optimizing a detector for a given SQUID as well as for given experimental boundary conditions, the geometry of the detector, i.e., the sensor area and height, as well as the concentration of magnetic ions within the sensor material can be arranged such that the influence of SQUID noise is minimized. However, in practice we most often want to read out an existing detector using a SQUID with given parameters. In this situation, we can't compensate for SQUID noise by adjusting the detector geometry. Consequently, we have to expect that the influence of SQUID noise on the energy resolution is stronger than for optimized detectors. Equivalent to an optimized detector, it turns out that the energy resolution increases with the SQUID white noise level. This rise grows with the energy resolving power and is hence stronger for small detectors with small pickup coil inductance. For this reason, a detector that is optimized for measuring soft X-rays with very high precision requires a SQUID with near quantum-limited noise performance to avoid a significant degradation of the energy resolution. Even a still very good SQUID having $\varepsilon_{c,w} \simeq 100\text{ }h$ increases the energy resolution of the detector by about a factor of 2 as compared to the intrinsic value.

As previously mentioned, state-of-the-art magnetic calorimeters usually employ a superconducting flux transformer to transduce the change of sensor magnetization into a change of magnetic flux inside the SQUID. The transfer function of the flux transformer,

$$\frac{\delta\Phi_S}{\delta\Phi} = \frac{M_{in}}{L_p + 2(L_{in} + L_w)}, \quad (4)$$

where $\delta\Phi_S$ and $\delta\Phi$ are the magnetic flux changes in the SQUID and the pickup coil, respectively, and M_{in} is the mutual inductance between the SQUID with inductance L_s and its input coil is influenced by parasitic inductances within the transformer circuit. These parasitic inductances arise, for example, from bonding wires that are used to connect the pickup coil of the detector to the input coil of the SQUID. A typical value for these wires is about $L_w = 500$ pH. While for detectors having a pickup coil inductance that exceeds several nH the degradation of the energy resolution usually hardly matters, the energy resolution is degraded by up to several 10% for a soft X-ray detector having usually a pickup coil inductance in the range of about 1 nH. Since $\delta\Phi_S/\delta\Phi \leq k_{in}/2\sqrt{L_s/L_p}$ for optimized coupling between detector and SQUID, i.e., $L_{in} = 0.5(L_p + 2L_w)$, the energy sensitivity referred to the pickup coil of the detector is increased at least by a factor $4/k_{in}^2$ compared to energy sensitivity of the SQUID leading to a stronger influence of the SQUID noise on the energy resolution of the detector. This might appear as a severe problem for the development of very high-resolution detectors that, in principle, can be overcome by using a detector geometry with direct flux coupling [1, 15, 16]. Here, the pickup coil of the detector and the SQUID loop are identical resulting in an enhanced flux coupling factor $\delta\Phi_S/\delta\Phi$ that can approach values up to 100%. Figure 3 (right) shows the calculated noise budget of an optimized soft X-ray detector with direct flux coupling assuming a SQUID with an intrinsic white noise contribution $\varepsilon_{s,w} = 2h$ as well as a $1/f$ -noise contribution with a corner frequency $f_c = 100$ Hz. Obviously, readout noise doesn't dominate the overall noise spectrum anymore and the detector performance is solely determined by the thermodynamical energy fluctuations, the sensor intrinsic $1/f$ excess noise contribution and the magnetic Johnson noise. In addition, the expected signal size is much larger due to the enhanced flux coupling between detector and SQUID.

Even though direct flux coupling therefore seems to be very well suited for building detectors reaching sub-eV energy resolution, there are some challenges that has to be overcome to actually build such a detector: (i) the power dissipation in the vicinity of the temperature sensor is higher due to parasitic SQUID Joule heating resulting in a potentially increase detector temperature with respect to the heat bath, (ii) parasitic effects such as SQUID resonances due to the capacitive coupling between sensor and SQUID might occur making the SQUID design more complex, and (iii) the increased signal size in combination with the very fast signal rise time of MMC might exceed the slew rate of state-of-the-art SQUID electronics, thus making it hard to follow the signal during its rise. Nevertheless, it has already been demonstrated that such a geometry can be implemented without significant disadvantages concerning SQUID or detector operation [15–17]. Due to the reduced influence of SQUID noise on the energy resolution of the detector, this configuration hence presents an interesting alternative to transformer-coupled detectors.

4 State-of-the-Art Metallic Magnetic Calorimeters

Nowadays, metallic magnetic calorimeters are being developed for a variety of applications. Depending on the actual use of the detector, different detector realizations exist. Nevertheless, all detectors have many things in common. This includes, for example, the method for preparing the persistent current inside the pickup coils generating the bias magnetic field as well as the technique for thermalizing the detector. To give an overview of these common features and to discuss the basic structure of a metallic magnetic calorimeter, we show in Fig. 4 colorized SEM pictures as well as microscope photographs of two state-of-the-art detectors.

A state-of-the-art metallic magnetic calorimeter consists of two meander-shaped or spiral-shaped pickup coils that are connected in parallel with the input coil of a current-sensing SQUID. As pointed out above, this configuration allows not only to read out two pixels by using only one SQUID but also to store a persistent current inside both pickup coils that creates the bias magnetic field being required for magnetizing the temperature sensor. The interconnections between both pickup coils are routed such that both pixels show signals with different polarity. For this reason, the polarity of the SQUID signal allows to distinguish in which absorber an event occurred. Another consequence of this wiring is that the detector forms a first-order gradiometer which cancels homogeneous variations of external magnetic background fields as well as fluctuations of the heat bath temperature. One interconnection between both pickup coils is equipped with a persistent current switch that allows to prepare a persistent current inside the pickup coils. The persistent current switch can be formed, for example, by a ‘U’-shaped extension that is covered with a heater. By actuating this heater, the underlying part of the superconducting circuit gets normal conducting. In this

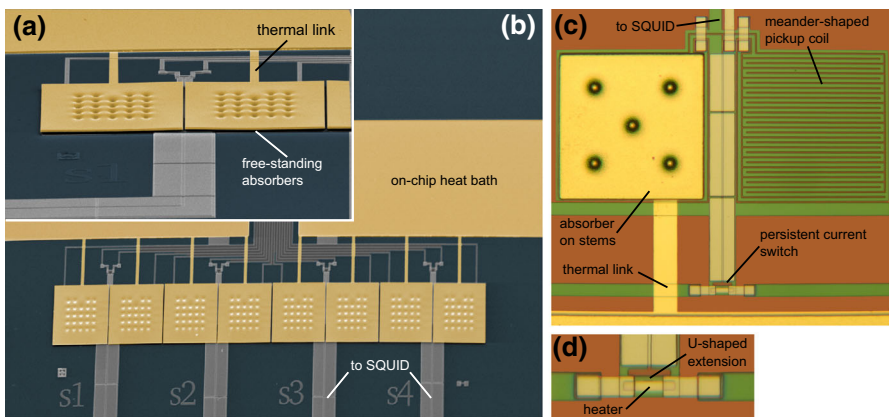


Fig. 4 Colorized SEM pictures as well as microscope photographs of the maXs-20 detector array having meander-shaped pickup coils and being optimized for high-resolution spectroscopy of photons with energy up to 20 keV [18] and a single-channel high-resolution detector that was developed for the ECHO experiment [19,20]. **a** Single two-pixel detector of the maXs-20 detector array. **b** Overview of the full maXs-20 detector array. **c** Overview of a single ECHO detector. **d** Magnification of the persistent current switch used within the ECHO detector (Color figure online)

situation, a current that is injected via terminals that are sitting on both sides of the persistent current switch can run through the pickup coils generating a magnetic flux that is given by the current strength and the inductance of both pickup coils. After closing the switch, the circuit gets superconducting again and the external current is slowly ramped down. To satisfy magnetic flux conservation inside the superconducting circuit, a persistent current is induced which creates the bias magnetic field. Alternative kinds of persistent current switches uses either superconducting bonding wires [21] or superconducting films with a critical temperature well below Nb [22,23] that both can be switched between a resistive and the superconducting state by changing the heat bath temperature.

On top of each meander-shaped pickup coil or between the spiral-shaped pickup coil and the superconducting ground plane, a paramagnetic temperature sensor is placed. The distance between sensor and pickup coil is kept as small as possible by using only a very thin insulation layer to guarantee strong inductive coupling. The detector is thermalized by connecting the temperature sensor to an on-chip heat bath that is formed by a several micrometer thick layer made of highly conducting, electroplated Au (see Fig. 4b). For this, a small normal conducting stripe runs between the on-chip heat bath and the temperature sensor (see Fig. 4c). Proper dimensioning of this stripe allows to precisely adjust the thermal conductance G of the link. The resulting decay time is given by $\tau_{\text{decay}} \simeq C_{\text{tot}}/G$ where C_{tot} denotes the total heat capacity of the detector. The particle absorbers sit on top of the sensors. They are often made of electroplated Au with a high residual resistivity ratio to allow for a fast internal equilibration of the absorber. The connection between absorber and sensor is realized by using several posts with a very small diameter (see Fig. 4a, c) such that the contact area between sensor and absorber is only a few percent. This greatly reduces the loss of athermal phonons in the initial stage of detector thermalization [9] that otherwise causes an asymmetric line broadening [13] and therefore allows to manufacture the detectors on a solid substrate. It is worth mentioning that introducing posts causes the absorbers to be free-standing. This, of course, makes the fabrication of the detectors challenging but simultaneously gives a huge flexibility in terms of detector design since the rise time of the detector can be precisely adjusted by dimensioning the number of posts as well as contact area between post and sensor.

5 State-of-the-Art Detector Performance

Since the first experimental demonstration of metallic magnetic calorimeters by Bandler et al. in 1993 [24] and the successful establishment of reliable microfabrication processes during the last decade, MMCs have become a mature technology and are nowadays routinely used for a variety of applications. As a result of the outstanding interplay between a highly sensitive temperature sensor and a near quantum-limited SQUID amplifier, they combine a very fast signal rise time, an excellent energy resolution, a large dynamic range and an almost ideal linear detector response. To summarize the state-of-the-art detector performance and to outline several key features of MMCs, we want to shortly discuss the performance of two maXs-20 detectors [18,25] that are optimized for the detection of soft X-ray photons.

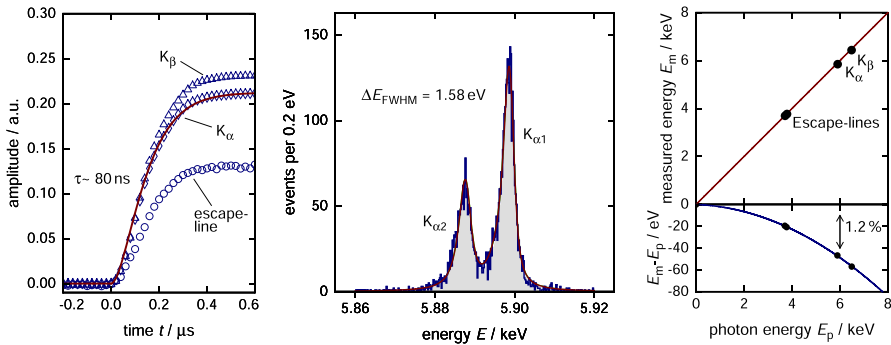


Fig. 5 (Left) Measured signal rise of three detector events belonging to different X-ray photons that are emitted by an ^{55}Fe source. The red solid line is a fit to one of the measured signal rises assuming that the shape follows an exponential rise with a time constant $\tau_{\text{rise}} \simeq 80 \text{ ns}$. (Middle) Energy spectrum of the K_α -line of an ^{55}Fe calibration source. While the blue histogram shows the measured spectrum, the gray area displays the intrinsic shape of the K_α -line. The solid red line is the expected lineshape when assuming an instrumental resolution of $\Delta E_{\text{FWHM}} = 1.58 \text{ eV}$. (Right) Measured energy E_m versus the photon energy E_p for different X-ray photons. Clearly, the detector shows an almost ideal linear detector response. The deviation $E_m - E_p$ follows a simple quadratic function (Color figure online)

Figure 5 (left) shows the measured signal rise of three detector events belonging to different X-ray photons that are emitted by an ^{55}Fe source as well as a fit to one of the measured signal rises assuming that the signal shape follows an exponential rise with a time constant $\tau_{\text{rise}} \simeq 80 \text{ ns}$. For the measurement we used a maXs-20 detector array having meander-shaped pickup coils that was operated at a temperature of $T = 30 \text{ mK}$. As already mentioned, the signal rise time is very fast and usually takes values $\tau_{\text{rise}} < 100 \text{ ns}$ [13, 21]. The fast rise results from the rapid internal thermalization within the sensor material due to the strong Korringa coupling between conduction electrons and spins [24]. It is given by $\tau_{\text{rise}} \simeq (1 - \beta)\kappa/T_{\text{el}}$ where β denotes the ratio between the heat capacity of the spins and the total heat capacity of the detector, κ is the Korringa constant of the sensor material and T_{el} is the temperature of the conduction electrons. Assuming, for example, an optimized detector ($\beta = 1/2$) having temperature sensors made of Au:Er ($\kappa_{\text{Au:Er}} = 7 \times 10^{-9} \text{ Ks}$ [26]) and which is operated at $T = 20 \text{ mK}$, we expect a signal rise time $\tau_{\text{rise}} < 200 \text{ ns}$. Furthermore, considering a detector with a certain sensitive area, stopping power and heat capacity, it turns out that metallic magnetic calorimeters are the fastest low-temperature microcalorimeters. In addition, the measurement presented here shows that the fast signal rise of MMCs is not slowed down by introducing stems between absorber and sensor to prevent the loss of athermal phonons during the initial phase of detector thermalization. Nevertheless, it is worth mentioning that the signal rise time can, in general, be freely adjusted to values above this intrinsic value by introducing a thermal bottleneck between absorber and sensor. In some cases for which the signal rise time doesn't matter, this helps to relax the readout requirements such as slew rate, readout bandwidth, and electronics speed.

Figure 5 (middle) shows the energy spectrum of the K_α -lines of an ^{55}Fe calibration source as measured with a maXs-20 detector having spiral-shaped pickup coils with a superconducting ground plane on top of the sensor [25]. The operating temperature

of the detector was 13 mK. In addition to the intrinsic line shape of the K_α -line (gray area), a fit to the measured spectrum is shown assuming a Gaussian line broadening with an instrumental energy resolution of $\Delta E_{\text{FWHM}} = 1.58$ eV. The energy resolving power of this detector is hence $E/\Delta E_{\text{FWHM}} > 3600$ and almost reaches the resolving power of state-of-the-art crystal spectrometers while covering at the same time a very much larger energy bandwidth. Thanks to the introduction of the stems between sensor and absorber, a loss of athermal phonons is avoided. Therefore, the broadening of the intrinsic line shape due to the finite energy resolution of the detector is symmetric, i.e., there is no low-energy tail as previously observed for many detectors that were structured on solid substrate. This greatly simplifies the fabrication process of the detectors since manufacturing detectors on membranes or introducing similar structures for avoiding athermal phonon loss can be omitted.

Figure 5 (right) shows the measured energy E_m versus the photon energy E_p for soft X-ray photons having different energies. Clearly, the detector shows an almost ideal linear detector response. The deviation $E_m - E_p$ from the ideal linear detector response follows a simple quadratic function and is only 1.2% for 5.9 keV photons. Therefore, the calibration of the detector is rather easy and only requires the acquisition of a small number of calibration lines with well-known energy to calibrate the detector over the full energy range. In addition, as long as the bias field or the detector temperature is not altered, the calibration doesn't change and remains valid for the entire measurement. This is somehow different for other kind of detectors such as TESs for which changes in the superconducting transition, for example, due to phase slips can alter the energy calibration over time and thus requires a continuous calibration during the full measurement time.

Figure 6 shows the energy spectrum of an ^{241}Am calibration source as measured with the maXs-20 detector. Since the detector is optimized for detecting soft X-ray

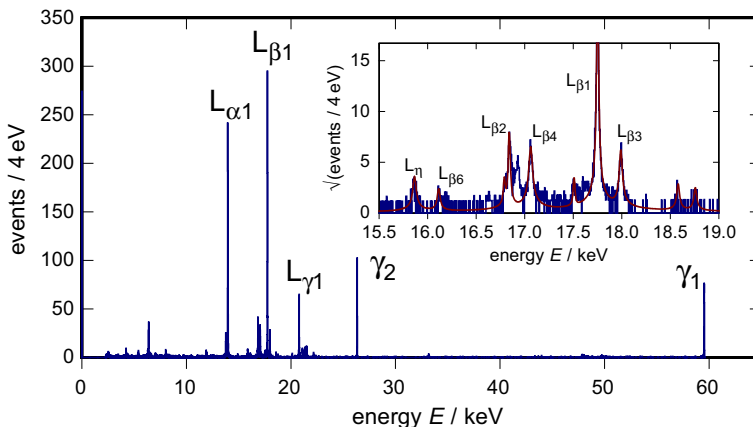


Fig. 6 Energy spectrum of an ^{241}Am calibration source as measured with a maXs-20 detector that is optimized for detection soft X-ray photons. The inset shows the energy range between 15.5 and 19 keV in more detail. The γ -labels within the spectra indicate nuclear transitions ^{241}Am , while the L-lines indicate different fluorescence lines of the daughter nuclide ^{237}Np . The solid red line within the inset shows a fit to the measured spectrum (Color figure online)

photons, we operated the detector for this particular measurement in an energy range for which it was not foreseen. We therefore have to expect that the measured line intensities have to be corrected for the quantum efficiency of the detector which significantly drops for energies above 10 keV. Nevertheless, this spectrum clearly shows that the detector output doesn't saturate, even if the detector is used for detecting particles with energies much higher than the detector was designed for. For this reason, a small high-resolution soft X-ray detector can be used, for example, to determine a line-splitting at high X-ray energies with very high accuracy. Combining the data from soft and hard X-ray detector thus allows to measure the line intensities, positions and splittings with very high precision.

When using a soft X-ray detector for measuring hard X-rays, we have to expect that the nonlinearity is larger and doesn't follow a simple quadratic function. In general, the nonlinearity of a metallic magnetic calorimeter results from the fact that the total heat capacity C_{det} of the detector and the magnetization M of the paramagnetic sensor depend on temperature which is altered by the absorption of the energy E . When a detector with small heat capacity is used for detecting hard X-ray photons the temperature excursion can be rather high. To give an example, we want to calculate the expected temperature increase when stopping a 5.9 keV and a 59 keV in a soft X-ray detector having a heat capacity in the range of 1 pJ/K at an operation temperature of 20 mK. The temperature increase for a 5.9 keV photon is about 1 mK. The temperature excursion is therefore only about 5% of the bath temperature, and the detector basically stays in its linear range. However, for a 59 keV photon the temperature increase is about 10 mK assuming a temperature independent heat capacity of the detector. We hence see that the detector temperature significantly exceeds the heat bath temperature and the temperature dependence of the thermodynamical detector properties has to be taken into account. This can be done by Taylor series expansion of the detector signal $\delta\Phi_s \sim \delta\Phi(T(E))$ where $\delta\Phi_s$ denotes the measured flux signal and $\delta\Phi$ is the magnetic flux change in the pickup coil. Including second order terms, we get the following expression for the deviation from the ideal linear detector response:

$$\Delta\Phi_s(E) \simeq \frac{1}{C_{\text{det}}(T_0)} \frac{\partial\Phi}{\partial T} E + \frac{1}{2} \left[\frac{1}{C_{\text{det}}(T_0)} \frac{\partial}{\partial T} \frac{\partial\Phi}{\partial E} - \frac{1}{C_{\text{det}}(T_0)^2} \frac{\partial\Phi}{\partial E} \frac{\partial C_{\text{det}}}{\partial T} \right] E^2 \quad (5)$$

Figure 7 shows the measured energy E_m versus the photon energy E_p for different strong peaks within the ^{241}Am spectrum (see Fig. 6) as well as the deviation of the measured energies from the known photon energies when using a 2nd or 3rd order polynomial fit of the $E_m(E_p)$ dependence. Furthermore, the residuals of the used calibration lines are shown for both cases. Obviously, the residuals are relatively large when using only a 2nd-order polynomial fit and the 3rd-order corrections improves the line accuracy quite a lot. At this point we want to mention one more time that this measurement was performed with a soft X-ray detector that was illuminated by hard X-rays. Therefore, the fact that a simple 3rd order correction of the nonlinearity is sufficient to determine the position of a line with a accuracy of about 1 eV is tremendous.

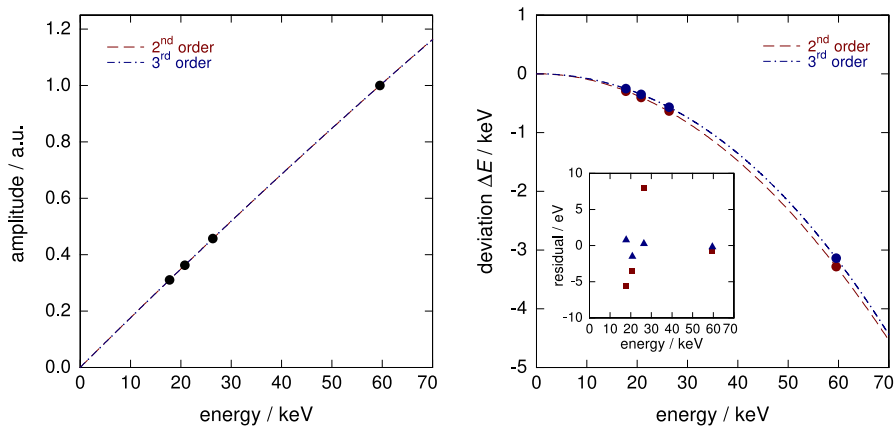


Fig. 7 (Left) Measured energy E_m versus the photon energy E_p for different strong peaks within the ^{241}Am spectrum. The dark red and blue lines indicate a 2nd- or 3rd-order polynomial fit of the dependence $E_m(E_p)$. (Right) Deviation of the measured energies from the known photon energies when using a 2nd- or 3rd-order polynomial fit of the $E_m(E_p)$ dependence. The inset shows the residual of the used calibration lines for both cases (Color figure online)

6 Summary and Outlook

This paper gave an overview of the state of the art of metallic magnetic calorimeters. We have shown that MMCs are particularly suited for a variety of applications due to their fast signal rise time, their excellent energy resolution, the large energy bandwidth as well as the rather small deviation from an ideal linear detector response. Moreover, microfabrication techniques are mature technology and allow to build detector arrays consisting of several thousands of virtually identical detectors. The measured signal rise times are well below 100 ns for state-of-the-art detectors and the presently achieved energy resolution at 5.9 keV is $\Delta E_{\text{FWHM}} = 1.58 \text{ eV}$. We expect that next generation devices, e.g., using direct flux coupling, reach energy resolutions below 1 eV.

Acknowledgements We would like to thank our colleagues for many stimulating and fruitful discussions as well as the participation in different experiments. We also would like to thank T. Wolf as well as the KIP cleanroom team for technical support during device fabrication. The work was partially performed in the framework of the DFG research unit FOR2202 (funding under En299/7-1 and Ga2219/2-1) as well as the European Microkelvin Platform EMP. Furthermore, we greatly acknowledge funding by the German Federal Ministry of Education and Research (funding under Grant BMBF 05P12VHFA5) as well as by the European Unions Horizon 2020 research and innovation program (funding under Grant agreement 664732).

References

1. A. Fleischmann et al., Metallic magnetic calorimeters, in *Cryogenic Particle Detection*, vol. 99, Topics in Applied Physics, ed. by C. Enss (Springer, Berlin, 2015)
2. K.D. Irwin et al., Transition-edge sensors, in *Cryogenic Particle Detection*, vol. 99, Topics in Applied Physics, ed. by C. Enss (Springer, Berlin, 2015)
3. D. McCammon et al., Semiconductor thermistors, in *Cryogenic Particle Detection*, vol. 99, Topics in Applied Physics, ed. by C. Enss (Springer, Berlin, 2015)

4. P. Rider et al., Trans. Metall. Soc. Aime **233**, 14881496 (1965)
5. A. Abragam et al., *Electron Paramagnetic Resonance of Transition Metals* (Claredon Press, Oxford, 1970)
6. G. Williams et al., Phys. Rev. **185**, 407414 (1969)
7. W. Hahn, Physica B **180/181**, 176178 (1992)
8. L. Tao et al., Phys. Rev. B **4**, 301 (1971)
9. C. Enss et al., J. Low Temp. Phys. **121**, 137176 (2000)
10. B.L. Zink et al., J. Appl. Phys. **99**, 08B303 (2006)
11. A. Burck et al., J. Low Temp. Phys. **151**, 337–344 (2008)
12. S.T.P. Boyd et al., AIP Conf. Proc. **1185**, 595–598 (2009)
13. A. Fleischmann et al., AIP Conf. Proc. **1185**, 571–578 (2009)
14. S. Kempf et al., Supercond. Sci. Technol. **28**, 045008 (2015)
15. V. Zakosarenko et al., Supercond. Sci. Technol. **16**, 1404–1407 (2003)
16. R. Stolz et al., IEEE Trans. Appl. Supercond. **15**, 773–776 (2005)
17. S.T.P. Boyd, et al. These Proc. (2017)
18. C. Pies et al., J. Low Temp. Phys. **167**, 269–279 (2012)
19. S. Kempf et al., J. Low Temp. Phys. **176**, 426–432 (2012)
20. L. Gastaldo et al., Eur. Phys. J. Spec. Top. **226**, 1623–1694 (2017)
21. H. Rotzinger et al., J. Low Temp. Phys. **151**, 351–356 (2008)
22. R. Hummatov et al., IEEE Trans. Appl. Supercond. **27**, 2200205 (2017)
23. S.R. Kim et al., J. Low Temp. Phys. **184**, 356–362 (2016)
24. S.R. Bandler et al., J. Low Temp. Phys. **93**, 709–714 (1993)
25. A. Fleischmann, et al., in Preparation (2017)
26. M.E. Sjöstrand et al., Phys. Rev. B **11**, 3292–3297 (1975)